An L-band geophysical model function for SAR wind retrieval using JERS-1 SAR

doi: 10.1109/TGRS.2003.808836

An L-Band Geophysical Model Function for SAR Wind Retrieval Using JERS-1 SAR

Teruhisa Shimada, Hiroshi Kawamura, *Member, IEEE*, and Masanobu Shimada, *Member, IEEE*

***Abstract*—An L-band geophysical model function is developed using Japanese Earth Resources Satellite-1 (JERS-1) synthetic aperture radar (SAR) data. First, we estimate the SAR system noise, which has been a serious problem peculiar to the JERS-1 SAR. It is found that the system noise has a feature common in all the SAR images and that the azimuth-averaged profile of noise can be expressed as a parabolic function of range. By subtracting the estimated noise from the SAR images, we can extract the relatively calibrated ocean signals. Second, using the noise-removed SAR data and wind vector data from the NASA Scatterometer and buoys operated by the Japan Meteorological Agency, we generate a match-up dataset, which consists of the SAR sigma-0, the incidence angle, the surface wind speed, and wind direction. Third, we investigate the sigma-0 dependence on incidence angle, wind speed, and wind direction. While the incidence angle dependence is negligible in the present results, we can derive distinct sigma-0 dependence on wind speed and direction. For wind speeds below 8 m/s, the wind direction dependence is not significant. However, for higher wind speeds, the upwind–downwind asymmetry becomes very large. Finally, taking into account these characteristics, a new L-band-HH geophysical model function is produced for the SAR wind retrieval using a third-order harmonics formula. Resultant estimates of SAR-derived wind speed have an rms error of 2.09 m/s with a negligible bias against the truth wind speed. This result enables us to convert JERS-1 SAR images into the reliable wind-speed maps.**

***Index Terms*— Japanese Earth Resources Satellite-1 synthetic aperture radar (JERS-1 SAR), L-band model function, synthetic aperture radar (SAR) wind retrieval.**

I. Introduction

COASTAL surface winds are one of the most important factors that control the sea state and the upper layer circulation in coastal seas. Coastal surface winds are strongly influenced by the coastal features, i.e., land topography, land constituents, coastlines and land/sea thermal conditions. It is quite difficult to map coastal surface winds with sufficiently high temporal and spatial resolution to meet the increasing needs for such data.

Synthetic aperture radar (SAR) has an imaging capability of the normalized radar cross section (NRCS) with quite a high spatial resolution. It has been proven that the SAR image can be converted into the high-resolution surface wind speed map by using the same wind retieval model as used for the scatterometer (e.g., see [1]). Recently, SAR imagery became available for researchers and applications due to long persisting operation of SARs onboard European Remote Sensing 1 and 2 (ERS-1/2), Japanese Earth Resources Satellite-1 (JERS-1), and RADARSAT. In the near future, more SAR imagery will be provided by new satellites, i.e., ENVISAT (Environmental Satellite), ALOS (Advanced Land Observing Satellite) and RADARSAT2.

At present, C-band SARs of ERS-1/2 and RADARSAT have been used for SAR wind retrieval, which is due to the existence of C-band model function for the surface wind retrieval. Many studies have revealed the efficiency of SAR-derived wind fields for interpreting various atmospheric and oceanic phenomena (e.g., see [2]–[6]). However, JERS-1 SAR data have not been used due to a lack of L-band model function.

In order to retrieve surface wind fields from SAR imagery, three conditions have to be satisfied. First, each pixel value of the SAR imagery, which is equivalent to the NRCS, must be calibrated absolutely or relatively for wind retrieval. Second, a geophysical model function (GMF) has to be established for the SAR microwave band. A GMF relates the radar backscattering intensity to the sea surface winds with parameters of microwave frequency, polarization, and sensor/sea-surface geometry. For the SAR wind retrieval, we need to specify the wind direction through the other data sources because SAR has only one-look direction. In other words, the SAR provides only the wind speed with very high spatial resolution ($10 \sim 100$ m). Previous studies on the SAR wind retrieval have used the wind directions from satellite scatterometers, *in situ* ship/buoy measurements, and operational/nonoperational meteorological model outputs. On the other hand, the azimuth cut-off method is examined for wind retrievals using the combination of interlaced wind scatterometer and high-resolution SAR wave mode imagettes provided by ERS-1/2 [7].

JERS-1 SAR has been operated with reduced transmitted power (325 W nominal) instead of the normal transmitted power (1300 W nominal) since September 18, 1992 in order to cope with the degradation of the azimuth antenna pattern. Hence, the sensitivity is 6 dB smaller than the original design, which has degraded the noise equivalent sigma-0 to -14.5 dB. Due to the lower SNR, it is possible that the range of fluctuation of speckle noise exceeds the lower signal level. In terms of the sensor calibration, it is difficult to subtract the system noise from SAR data to prevent the received power from seeming negative. Because the noise influence on the SAR image of ocean is not negligible, we cannot consider the digital pixel values of the whole image as calibrated backscatter.

A GMF for L-band horizontal (HH) polarization has not been developed yet. Characteristics of L-band backscattering at the

Manuscript received June 12, 2002; revised September 5, 2002.

T. Shimada and H. Kawamura are with the Center for Atmospheric and Oceanic Studies, Faculty of Science, Tohoku University, Sendai, Miyagi 980-8578, Japan (e-mail: shimada@ocean.caos.tohoku.ac.jp).

M. Shimada is with the Earth Observation Research Center, National Space Development Agency of Japan, Tokyo 104-6023, Japan (e-mail: shimada@eorc.nasda.go.jp).

Digital Object Identifier 10.1109/TGRS.2003.808836

sea surface are not well understood for wide ranges of the parameters. Several studies suggested that the NRCS of L-band depends on both the wind speed and the wind direction [8]–[10]. Researchers using the SEASAT SAR pointed out that an L-band SAR image could be transferred into a high-resolution wind map using the relationship between the NRCS and the wind vector [11], [12].

In the present study, an L-band GMF is developed for SAR wind retrieval using the L-band SAR of JERS-1. First, we investigate the system noise of JERS-1 SAR images to conduct relative calibration of each pixel value to the NRCS. Next, using the noise-removed data, we make a match-up dataset composed of the NRCS, incidence angle, wind speed, and wind direction. The coincident and collocated wind vector data are obtained from the NASA Scatterometer (NSCAT) and moored buoys operated by the Japan Meteorological Agency (JMA). These are described in Section II. In Section III, we investigate the dependence of L-band NRCS on incidence angle, wind speed, and wind direction. Then on the basis of those results, the L-band GMF is developed. Finally, we apply this L-band GMF to JERS-1 SAR images to retrieve wind fields for examination of the GMF and the resultant SAR-derived wind speed. Section IV is devoted to discussion. Summary and conclusions are given in Section V.

II. Data and Method

A. JERS-1 SAR, NSCAT, and JMA Buoy Data

In order to investigate L-band backscattering characteristics, we used the JERS-1 SAR, NSCAT onboard ADEOS-I, and *in situ* observations from the moored buoys of the JMA. Surface wind vectors of the NSCAT and the JMA buoys are used as sea truth data. A unique point of the present study is usage of the NSCAT vector winds for characterization of the JERS-1 SAR signals. Both ADEOS and JERS-1 had sun-synchronous orbits, whose orbital factors are close to each other. Moreover, the local times at descending node of the two satellites are around 10:30 A.M. Therefore, if the observation swath of NSCAT completely or partially contains that of JERS-1 SAR and the observation times are close, we can obtain many series of coincident and collocated observations along the swath path. In such a case, temporal difference between observations by two sensors is less than 30 min. In analogy to the synergetic (NSCAT and JERS-1 SAR) approach taken in this paper, ERS-1 and 2 scatterometer and SAR during the tandem phase are used for a validation of wind retrieval from SAR, by which high-latitude ocean areas were covered with a 30-min separation time [13].

JERS-1 was launched on February 11, 1992. An L-band and HH polarization SAR onboard JERS-1 featured a high resolution of 18 m, a fixed off-nadir angle of 35°, and an imaging width of 75 km. We collected 2288 scenes of its observations, which cover the seas around Japan, i.e., the Japan Sea, the East China Sea, and the northwestern North Pacific Ocean. They are made up of 2101 scenes with corresponding NSCAT observations and 187 with corresponding JMA buoy observations. Fig. 1 shows coverage of JERS-1 SAR observations utilized in this study. Most of the JERS-1 images used in the present study captured the area of the open ocean, and all the match-ups

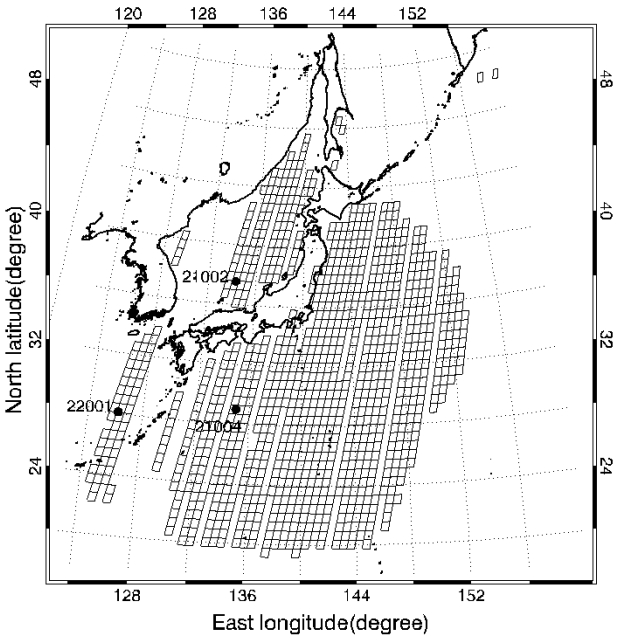

Fig. 1. Map of coverage of JERS-1 SAR observations utilized in this study and the location of JMA buoys (WMO buoy nos. 21 002, 21 004, and 22 001).

are generated for offshore regions because of the corresponding NSCAT wind vectors, which cannot be retrieved in the nearshore seas. Therefore, influence of the coastal seas on the radar backscattering, such as effects of depth fluctuations, currents, slicks, and fetch on the surface waves, may not be serious. Raw SAR data are processed by the Sigma SAR Processor [14] to generate slant-range images for the analysis of the present study.

The Advanced Earth observing Satellite (ADEOS) was launched on August 17, 1996 and carried eight sensors including NSCAT until June 30, 1997. NSCAT is a dual-swath Ku-band scatterometer that can measure vector winds over a swath of 600 km with a spatial resolution of 50/25 km. The NSCAT Ocean Data product used in this study is 25-km Selected Wind Vector (SWV). It contains the surface wind vectors selected along the satellite track with a spatial resolution of 25 km and flags.

JMA operates three Ocean Data Buoy Stations (WMO buoy nos. 21 002, 21 004, and 22 001) in the seas around Japan. Fig. 1 shows their locations. They measure 11 meteorological and oceanic variables including the wind direction and speed. In order to make the buoy winds compatible with the NSCAT winds, the buoy wind speeds measured at 7.5 m above sea surface are converted to the 10-m equivalent neutral wind speed by a method proposed in [15].

B. System Noise of JERS-1 SAR

Because it is quite difficult to derive absolutely calibrated NRCS of the ocean from the original JERS-1 SAR data due to the system noise, we carried out a relative calibration of the JERS-1 SAR signals for wind retrieval.

The slant-range image of JERS-1 SAR originally has 5888 pixels in the range direction and 5120 pixels in the azimuth direction. We cut off the left and bottom edges of the no-signal portions of the image and used 5388×4200 pixel sized image.

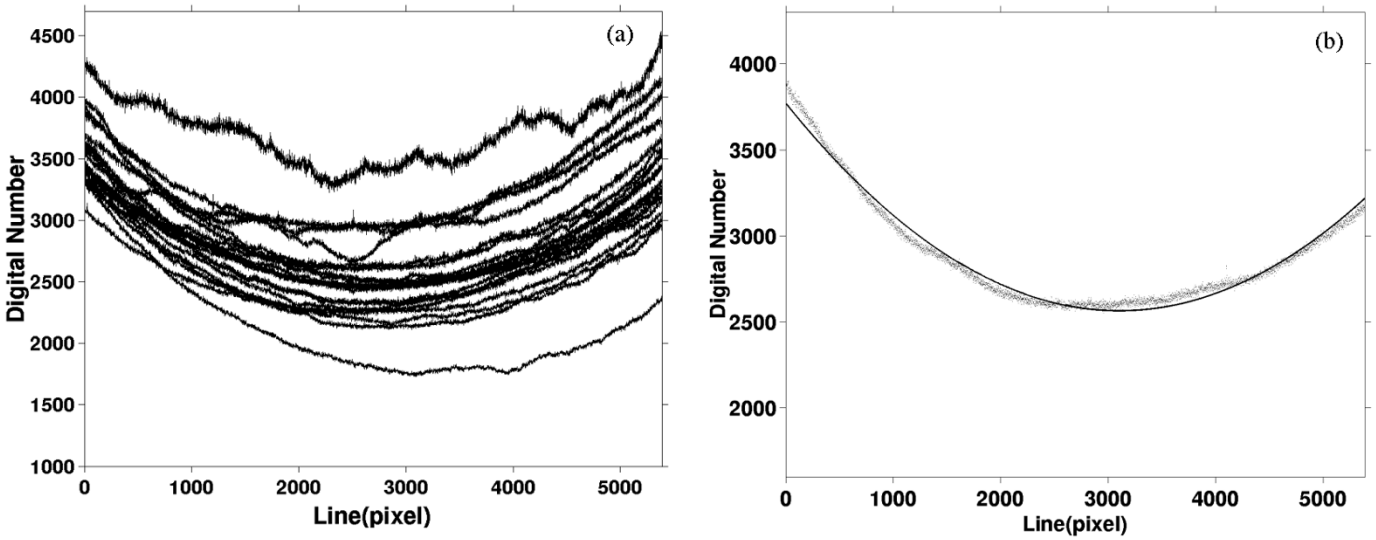

Fig. 2. (a) Comparison of range profiles of JERS-1 SAR image, which are averaged ove the azimuth direction. (b) A profile averaged over the azimuth direction of the slant range image (dotted line) anda regression curve of the parabolic function (solid line).

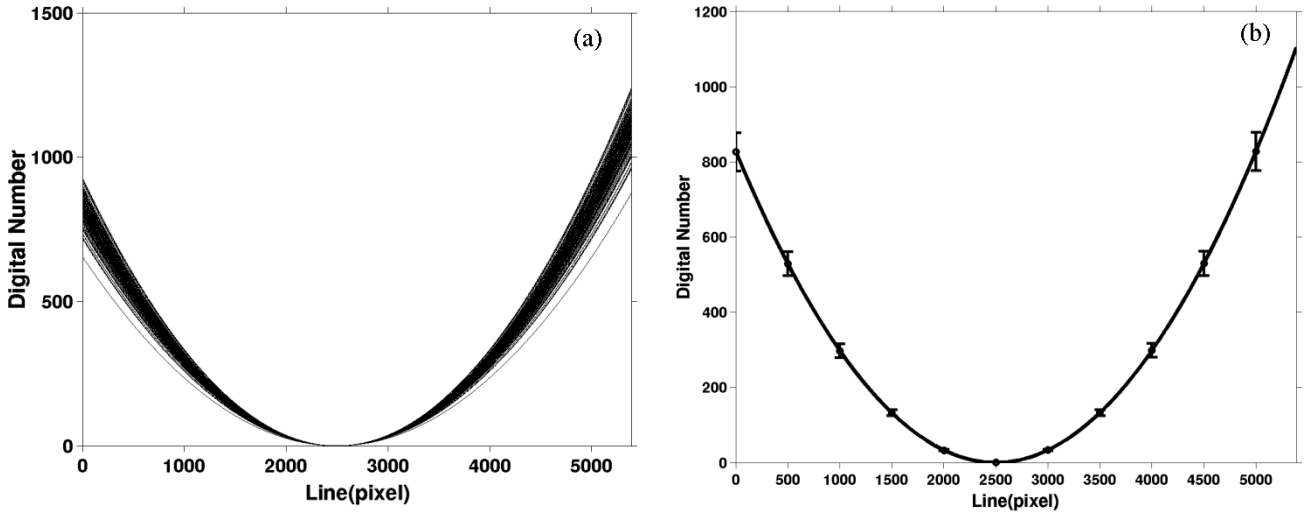

Fig. 3. (a) Comparison of range profiles. A vertex of every profile is moved to (2500,0). (b) Mean range profile averaged over each line. Error bars show the standard deviation.

It is known that JERS-1 SAR system noise exists in the range direction and is higher in the either side of center and lower in the center of the scene [16]. It suggests that the range-dependent noise remains after SAR calibration. Fig. 2(a) shows the azimuth-averaged profiles made from 20 SAR images. They are different from each other because the pixel value of the image is the sum of the signal from the ocean and the system noise. In order to examine the noise properties, we sampled 200 scenes of JERS-1 SAR and regress the azimuth-averaged profiles with a parabolic function based on the assumption that the system noise is linearly added to the ocean signals. Fig. 2(b) shows one example of the profile and the regression curve. We used the regression equation as

$$\mathrm{DN} = a(x-b)^2 + c \tag{2.1}$$

where DN is a digital value of a 16-bit image, and x is range with $x = 0$ corresponding to the far range. The regression coefficients are a, b, and c. Fig. 3(a) shows all profiles, whose vertexes are shifted to the same point of (2500,0). Fig. 3(b) shows the profile produced by averaging all the profiles in Fig. 3(a). Bars on the averaged profile indicate the standard deviations.

As can be seen in Fig. 3(a), most of the profiles are similar in shape. Actually, the standard deviation of coefficient a is very small (0.08×10^{-4}, i.e., 6% of the mean value of 1.32×10^{-4}). It can be concluded that the parabolic shape of profiles showing the JERS-1 SAR system noise is common to all the JERS-1 SAR images and that the system noise is a function of range. It is true that some profiles deviate from the regression curve, but this results from the natural phenomena captured by each scene. In Fig. 3(b), the variance is large on either side of center range because a small difference in coefficient a enhances the difference at both sides of the profiles.

The axis position of the parabolic function specified by the coefficient b distributes around the 3270th line. The coefficient b has a standard deviation of about 290. We conclude that the

location of the axis is different scene by scene. Therefore, in order to express the system noise as a function of range, the axis position for each scene needs to be computed through the regression. The reasons of the axis variations may be uncertainty of the JERS-1 orbital parameters and wind gradients in a scene.

We consider that the value of coefficient c depends on the wind speed, the wind direction, and the other ocean parameters.

On the basis of the above results, we express the system noise as a function of range. The value of coefficient a is set as the mean value 1.32×10^{-4}, which is defined as a_0. The axis position (b) of the parabolic function is estimated for each scene. We set a provisional value of c_0 at this moment. The c_0 value will be determined in Section II-C. Using these coefficients, the system noise (DNnoise) is expressed as

$$\text{DNnoise} = a_0 (x - b_i)^2 + c_0 \tag{2.2}$$

where b_i is the axis location of each scene. By subtracting the estimated system noise from all range lines of the SAR images, we reproduce the relatively calibrated images. Hereafter we use these modified digital values instead of the absolutely calibrated NRCS and refer to the square of the digital value as sigma-0 (σ^0_{lin}). The speckle noise is reduced enough for digital pixel values to always be positive after removing the system noise.

C. Match-Up Data

In this subsection, we describe the procedure to make a match-up dataset, which is composed of coincident and collocated observation variables. They are the JERS-1 SAR sigma-0 and incidence angle and the wind speed (U) and the wind direction (ϕ) from NSCAT and the JMA buoys. The wind direction is defined as the azimuth angle between the radar-looking direction and the surface wind direcion. In this study, in order to reduce the speckle noise, we define the SAR sigma-0 as a mean value of a 10-km ground square whose center is located at a geodetic position of wind vector cell of NSCAT or a buoy. In fact, sigma-0 averaged over an area larger than 10-km square varies little from a 10-km average. The10-km distance corresponds to 500–700 pixels in both the range and azimuth directions in the slant range image. Fig. 4 shows a scheme of match-up data generation. First, we consider the case of NSCAT. As described above, many match-ups are obtained when swaths of NSCAT and JERS-1 SAR overlap. An example of the overlapping swaths is shown in Fig. 5. One vector case among the wind vectors displayed in Fig. 4 corresponds to the use of JMA buoy data. The meteorological data observed by the JMA buoys at 3:00 UTC are used for the match-up generation because this acquisition time is closest to the local time of JERS-1 SAR passage. In order to reduce the influence of temporal variation of the buoy-observed wind, we exclude the data in case that the difference between 0:00 UTC and 3:00 UTC observation data is large. The difference thresholds are set at 1.5 m/s and 20° for the wind speed and direction, respectively. As a result, we have made 7577 match-ups, which are the sum of 7532 match-ups with NSCAT winds and 45 with JMA buoy winds. Fig. 6(a) and (b) shows the histograms of match-ups for the wind speed and direction, respectively.

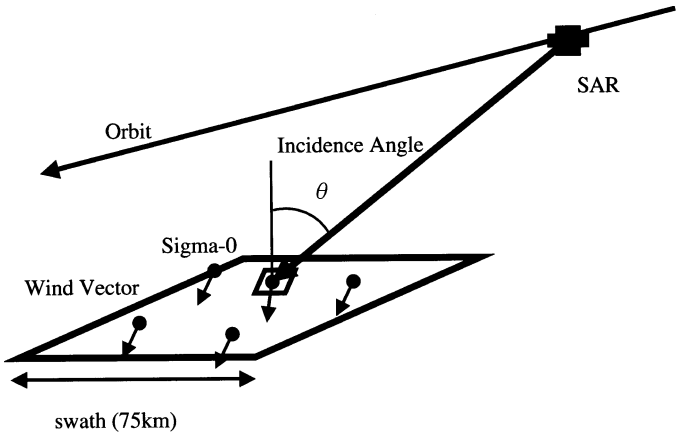

Fig. 4. Scheme of match-up data generation using wind vectors from NSCAT and JMA Buoys.

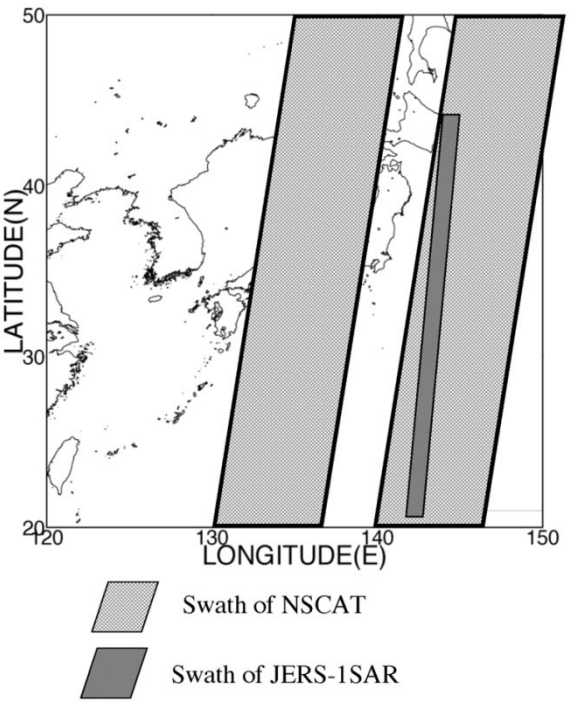

Fig. 5. Example of overlapping swaths of NSCAT and JERS-1 SAR (October 6, 1996).

Using the match-up dataset, we determine the consistent level of JERS-1 SAR system noise, i.e., c_0 in (2.2). In order to produce a reasonable L-band GMF, its continuity at 0 m/s has to be guaranteed. First, we make a match-up dataset using the provisional value $c_0 = 0$. Second, the match-ups are classified into bins of 1 m/s wind speed and 10° wind direction, and the outliers, which are defined as points that are more than twice the standard deviation from the mean value of each bin, are discarded. Thus, the minimum value among wind speed bins of 0–1 m/s is 2 250 000 in sigma-0, which corresponds to 1500 of 16-bit digital values. We redefine c_0 as that value, i.e., $c_0 = 1500$. By using this value, sigma-0 is also redefined in order that sigma-0 is zero when the wind speed is 0 m/s. Use of this value produces positive sigma-0 from the oceans and does not cause any problems in the following analyses and results.

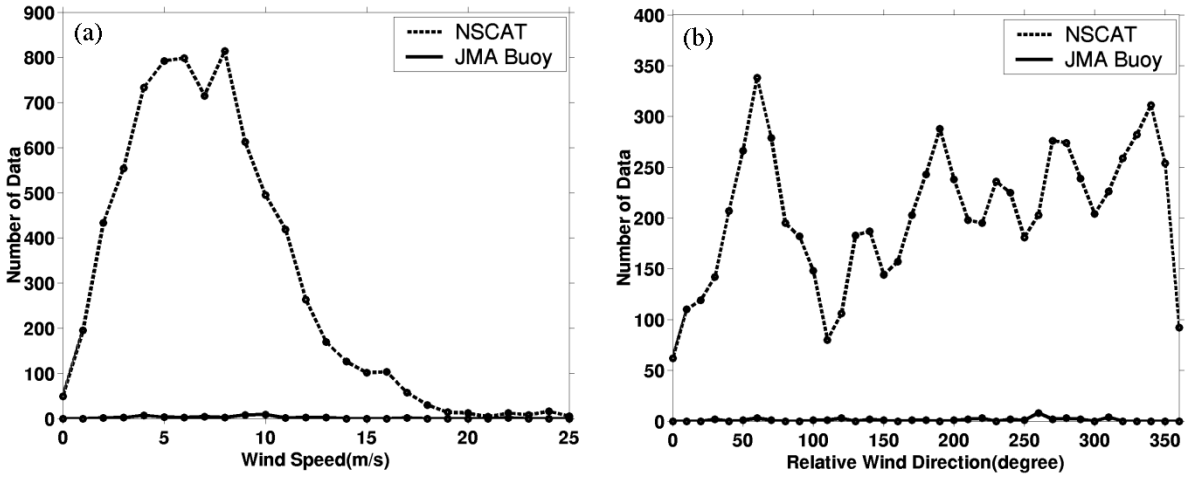

Fig. 6. Histograms of the number of match-ups for (a) wind speed and (b) wind direction.

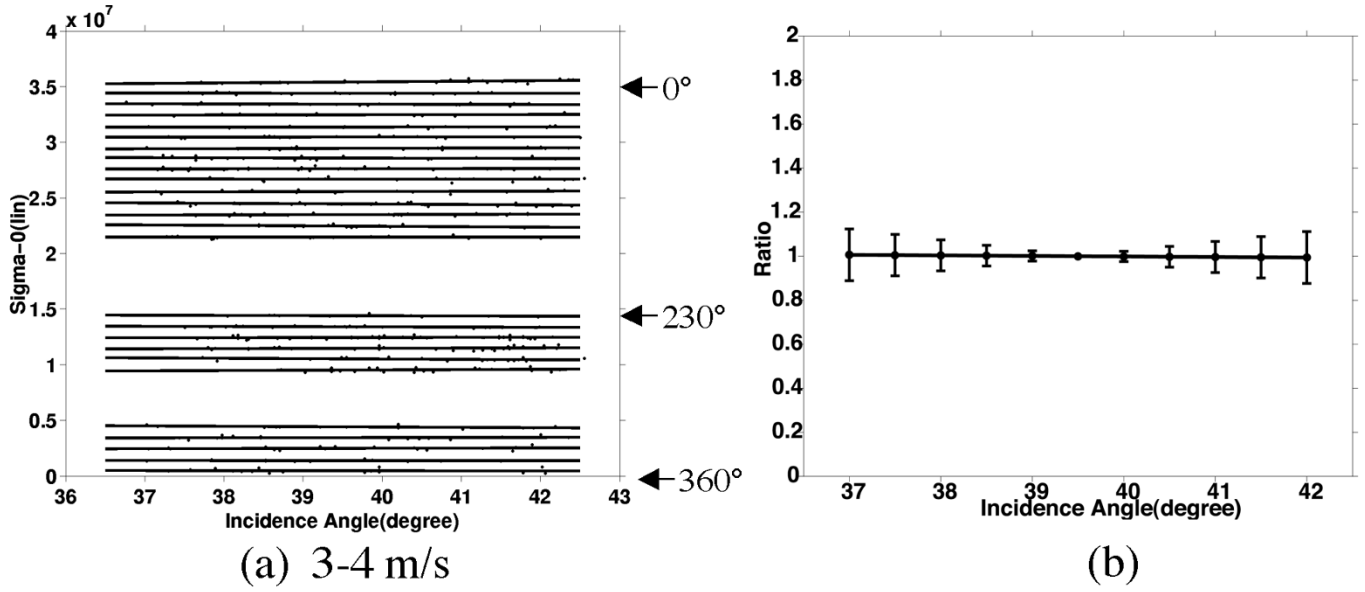

Fig. 7. Dependence of sigma-0 on incidence angle. (a), (c), and (e) show the incidence angle dependence for the wind-speed bins 3–4 m/s, 7–8 m/s, and 12–13 m/s, respectively. The plots and regression line are shown for the wind-direction bins containing the match-ups more than ten. The level of each wind-direction bin is offset for display of all the calculated regression lines in the figure. (b), (d), and (f) indicate the mean profiles normalized by sigma-0 at 39.5° with standard deviation for the wind-speed bins 3–4 m/s, 7–8 m/s, and 12–13 m/s, respectively.

In order to estimate the coefficients of the L-band GMF, a simple regression (no regression weights) is used in the analysis described in Section III. This is based on the assumption that NSCAT and buoy data are error-free sea truth.

III. Characteristics of L-Band Backscattering at the Sea Surface and L-Band GMF

A. Incidence Angle Dependence

The dependence of sigma-0 on incidence angle is examined for all the bins of wind speed and wind direction. The range of incidence angle varies from 37.0° to 42.0° within the SAR swath. Fig. 7(a), (c), and (e) shows the examples of the incidence angle dependence for all the bins of wind direction and the bins of wind speed 3–4 m/s, 7–8 m/s, and 12–13 m/s, respectively. Regression lines are also superimposed in the figures. The bins containing less than ten match-ups are excluded. The level of each wind-direction bin is offset for display of all the calculated regression lines in the figures. They have no significant inclination for the range of incidence angle. Furthermore, all the regression lines shown in Fig. 7(a), (c), and (e) are normalized by the sigma-0 at 39.5°, and then they are averaged over the incidence angle for each wind-speed bin. The resultant profiles with bars indicating standard deviation are shown in Fig. 7(b), (d), and (f), respectively. There is a slight inclination of the mean profile for the wind-speed bin of 12–13 m/s [Fig. 7(f)], but it should be noted that only six bins are available because of the small number of data for high wind speeds. They lie around one, which also indicates no incidence angle dependence for the range of incidence angle (37.0° to 42.0°). This is confirmed for the other bins, which are not shown here. Thus the dependence of incidence angle in the GMF is not considered in the follwing analyses.

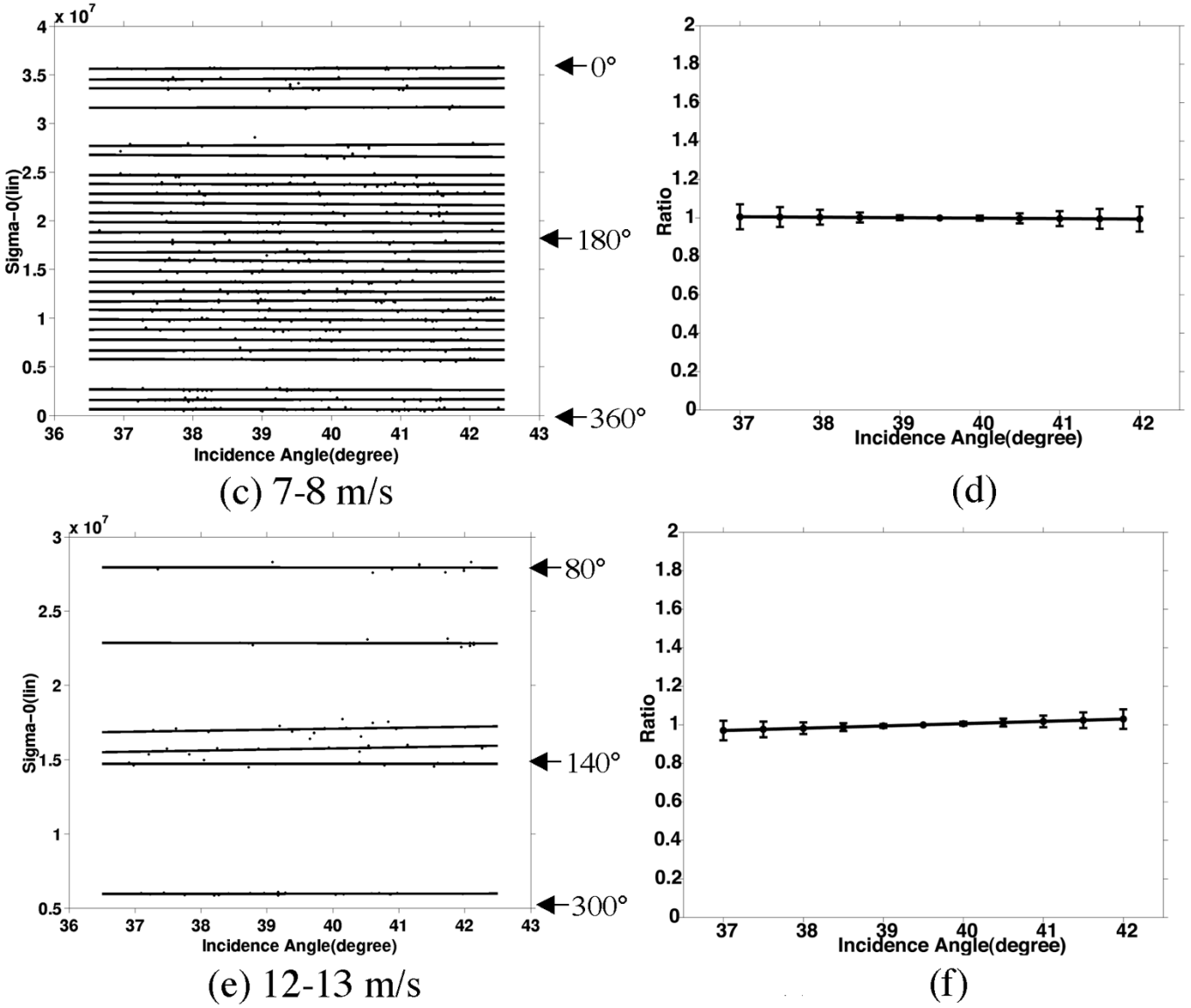

Fig. 7. *(Continued)* Dependence of sigma-0 on incidence angle. (a), (c), and (e) show the incidence angle dependence for the wind-speed bins 3–4 m/s, 7–8 m/s, and 12–13 m/s, respectively. The plots and regression line are shown for the wind-direction bins containing the match-ups more than ten. The level of each wind-direction bin is offset for display of all the calculated regression lines in the figure. (b), (d), and (f) indicate the mean profiles normalized by sigma-0 at 39.5° with standard deviation for the wind-speed bins 3–4 m/s, 7–8 m/s, and 12–13 m/s, respectively.

B. Wind Speed Dependence

The dependence of sigma-0 on wind speed is investigaed using the match-ups in the wind direction bins. Fig. 8 shows plots of sigma-0 versus the wind speed for wind directions of 0°, 50°, 90°, 140°, and 180°, which are center angles of the relative wind directions. Since the wind-speed dependences for the 180° to 360° bins are symmetric to those of 0° to 180°, we show the plots only for half of the wind-direction bins. Regression curves are also indicated in the figures. They are defined as a power law formula, which relates sigma-0 with the surface wind speed (e.g., see [17])

$$\sigma^0_{\rm lin} = 10^{\alpha} U^{\beta}. \tag{3.1}$$

The coefficient β is called "wind speed exponent," which indicates the sensitivity of sigma-0 to the wind-speed increase. The coefficients α and β are determined through regression of (3.1) against the match-up points.

In each wind direction bin, sigma-0 increases with the wind speed. The coefficient β is a variable of the wind direction. For the wind direction of 0° (upwind), sigma-0 has the largest increasing rate against the wind speed. The increasing rate decreases markedly, and the minimum increasing rate is seen at $\phi = 90°$ (crosswind), where sigma-0 has a tendency of saturation at the high wind speeds. Sigma-0 increases rather linearly with the wind speed for the wind direction of 180°(downwind). The wind speed exponents are 2.25, 0.50, and 1.18 at upwind, crosswind, and downwind, respectively.

C. Wind Direction Dependence

The dependence of sigma-0 on the wind speed is investigated for all the wind direction bins. Fig. 9 shows plots of sigma-0 versus the wind direction for the wind speeds from 0–1 m/s to

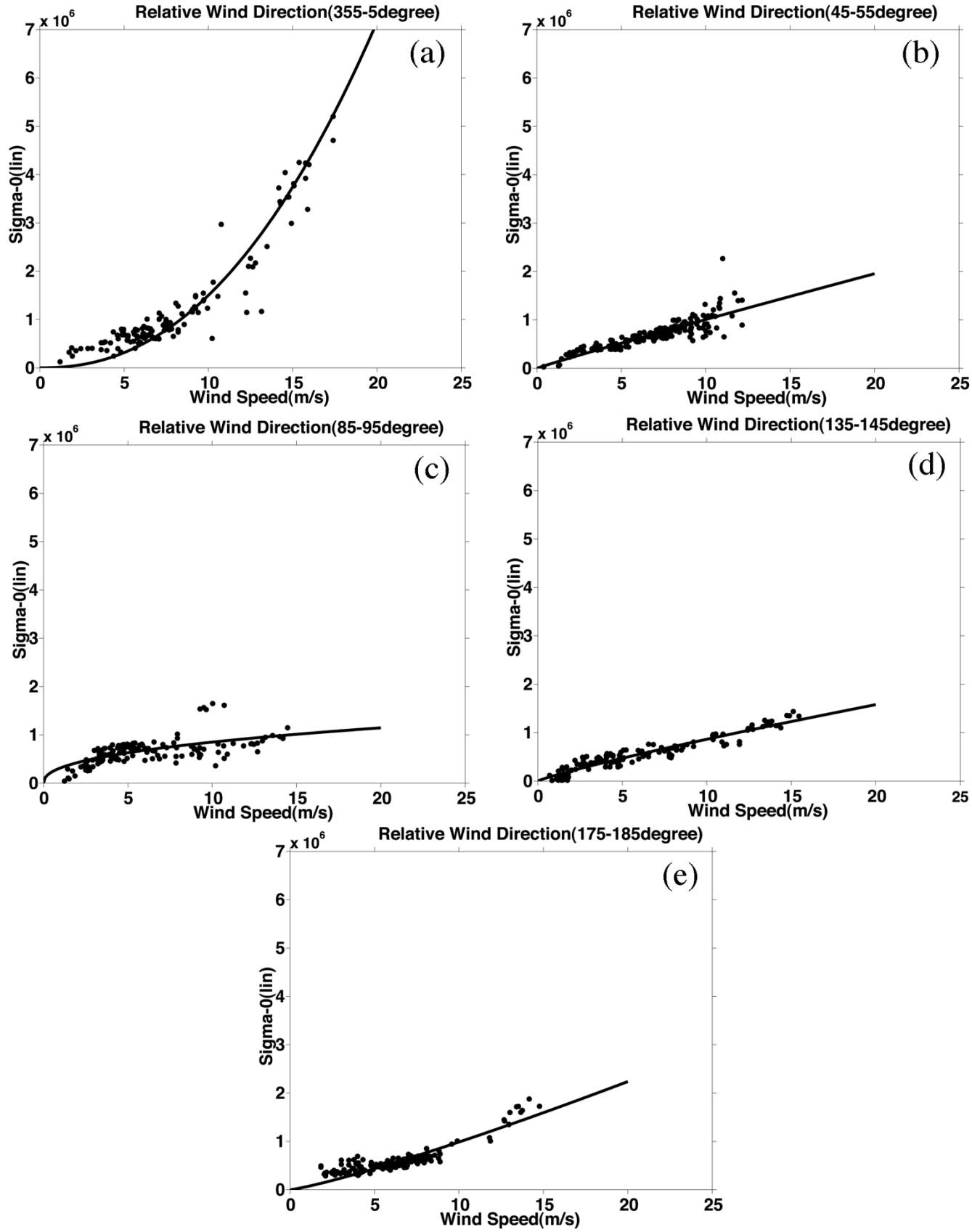

Fig. 8. Dependence of sigma-0 on wind speed for the relative wind direction of (a) 0°, (b) 45°, (c) 90°, (d) 135°, and (e) 180°. The regression lines are also shown.

19–20 m/s every other bin. In order to express the dependence of wind direction, second-order cosine harmonics formulas of the wind direction have been used by several researchers (e.g., see [17]–[19]). In the present case, the difference between the wind-

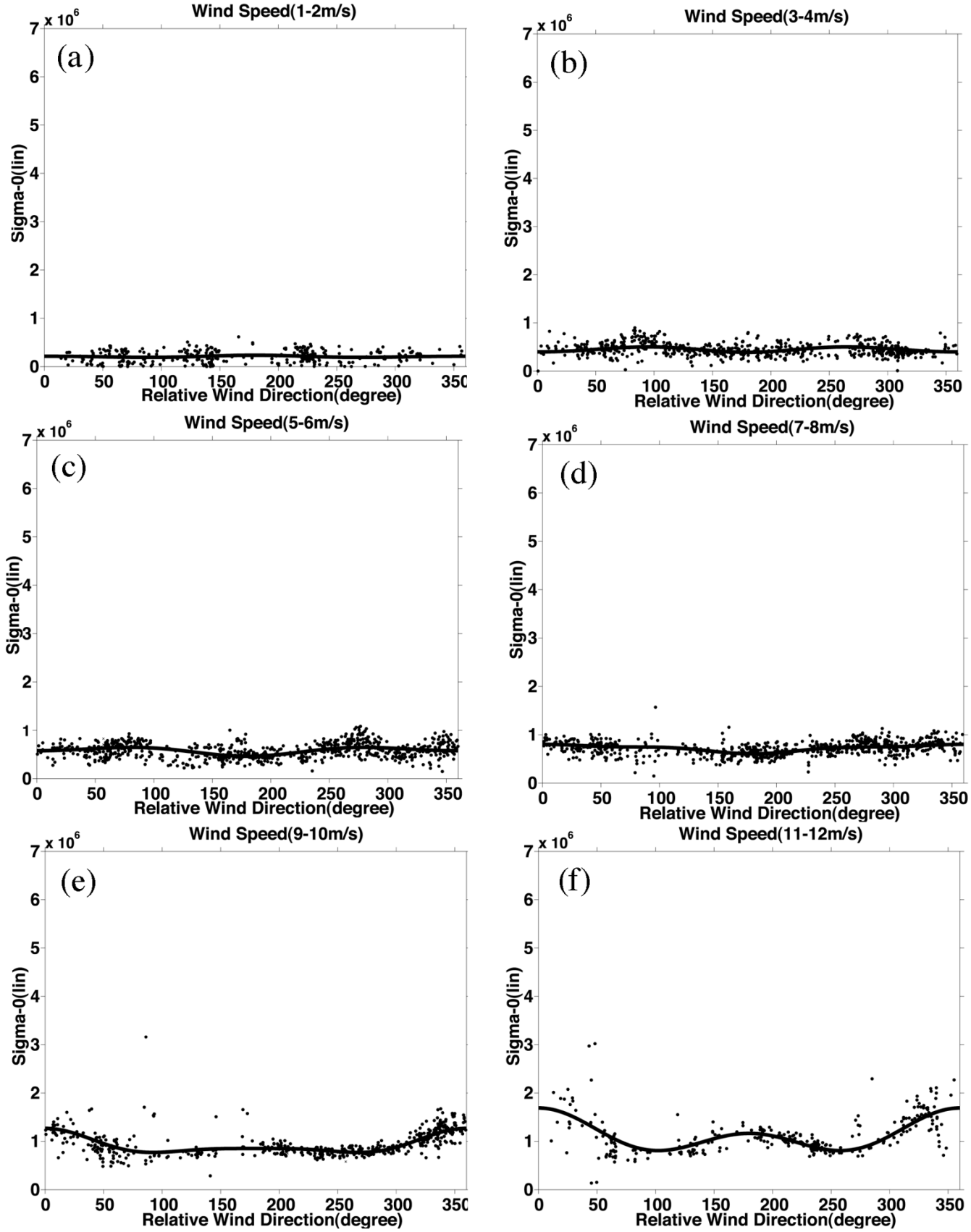

Fig. 9. Dependence of sigma-0 on wind direction for wind-speed bins (a) 1–2 m/s to (j) 19–20 m/s. Regression curves are also shown. For wind-speed bins of 15–20 m/s, the regression lines are computed by extrapolating wind speed dependence (see text).

speed dependences for upwind and downwind is large when the wind speed exceeds 10 m/s as seen in Section III-B. Therefore, conventional second-order harmonics formulas cannot express this deformed wind-direction dependence. In other words,

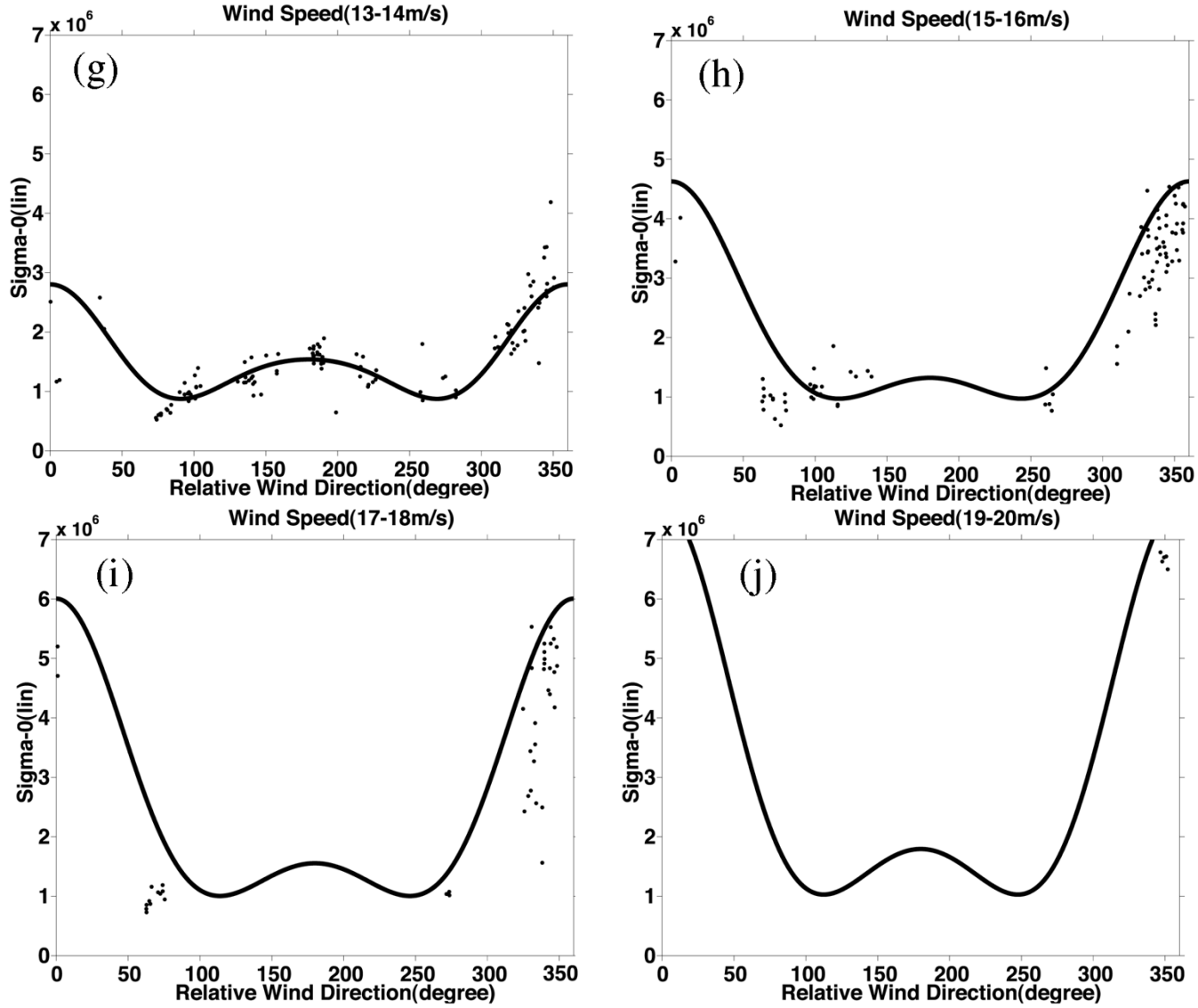

Fig. 9. *(Continued)* Dependence of sigma-0 on wind direction for wind-speed bins (a) 1–2 m/s to (j) 19–20 m/s. Regression curves are also shown. For wind-speed bins of 15–20 m/s, the regression lines are computed by extrapolating wind speed dependence (see text).

it cannot express the positions of the minimums at 90° and 270° and the large upwind–downwind asymmetry at the same time. For regression analyses, we adopt a third-order harmonic formula

$$\sigma^0_{\text{lin}}(U,\phi) = a_0(U) + a_1(U)\cos\phi + a_2(U)\cos 2\phi + a_3(U)\cos 3\phi. \quad (3.3)$$

a_i $(i = 0, 1, 2, 3)$ is the regression coefficient.

The signal level for the whole wind direction increases with wind speed. For a wind speed below 7 m/s [Fig. 9(a)–(c)], it can be concluded that the significant dependence on the wind direction does not exist, though the crosswind peak is systematically higher than the upwind and downwind peak. However, for the wind speed of 7–8 m/s, the upwind peak starts to dominate. For the wind speed of 9–10 m/s, the downwind peak also dominates following the upwind peak. When the wind speed becomes 11–14 m/s, the differences among the upwind peak and the downwind peak and the crosswind troughs become clearer, which continue toward higher wind speed.

For the wind-speed range of 15–20 m/s, because of a small number of the match-ups and their nonuniform distribution in the wind direction of each wind-speed bin, the regression analyses are less reliable. Therefore, in order to estimate better regression formula, we decide to extrapolate, toward the higher wind-speed range, the relation of wind speed dependence at $\phi = 0°$, 50°, 90°, 140°, and 180° shown in Fig. 8. Then, using the extrapolated values at these wind directions, the coefficients of harmonic formula are computed [the solid lines in Fig. 9(h)–(j)]. The determined curves for the high wind speeds do not conflict with the match-up plots in the figures.

D. L-Band GMF

We have developed an L-band GMF on the basis of the regression coefficients determined in Sections III-Ato III-C (Figs. 8 and 9). Considering no dependence on incidence angle in its

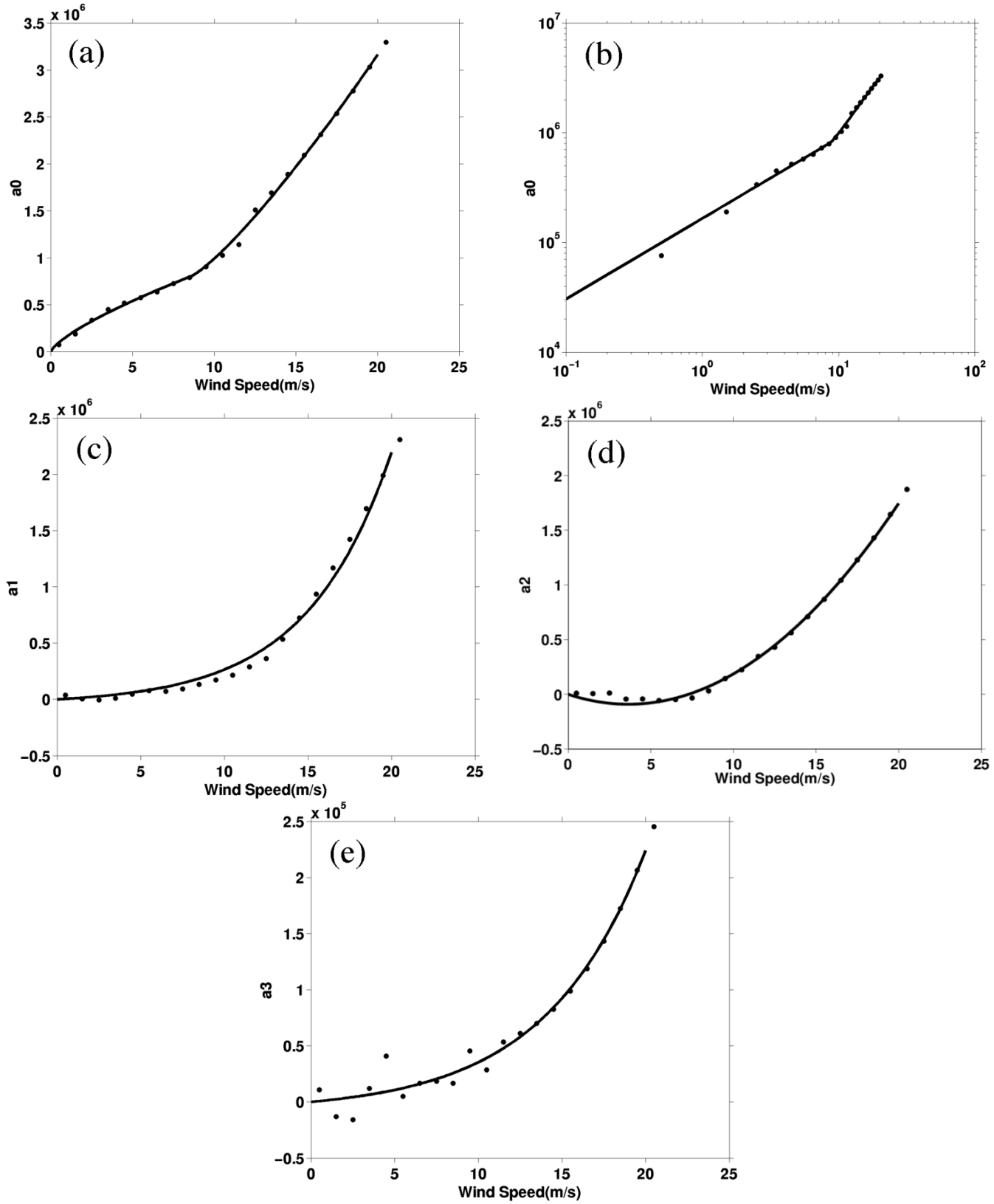

Fig. 10. Relationships between the regression coefficients and the wind speed. (a) a_0 and (b) a_0 in a logarithmic diagram, (c) a_1, (d)a_2, and (e) a_3. The curves representing behavior of the coefficients are also shown (see text).

range of present study (37.0° to 42.0°), the model derivation is then reduced to determining the wind speed dependence of the regression coefficients in (3.3). Fig. 10 shows the coefficients of the harmonic formulas (3.3) versus the wind speed. Fig. 10(a) shows that the relationship between the coefficient a_0 and the wind speed changes drastically at around $U = 8$ m/s. Fig. 10(b)

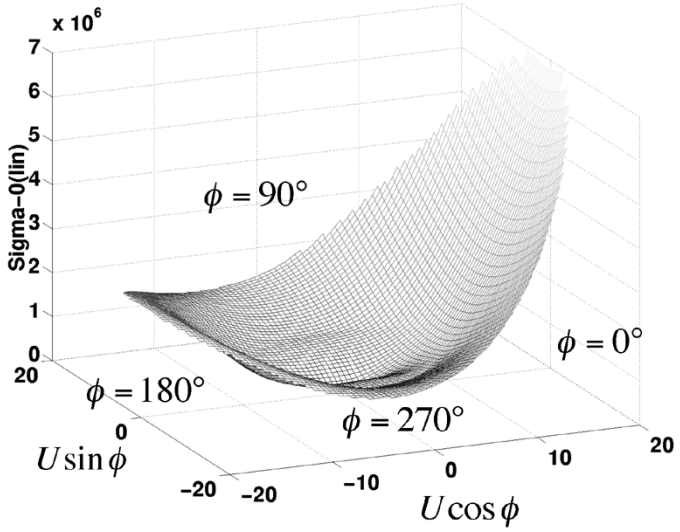

Fig. 11. Three-dimensional view of the L-band GMF.

shows the relationship in a logarithmic diagram. We represent the relationship by two lines as $\log_{10} a_0 = a + b \log_{10} U$, which are connected at $U = 8.5$ m/s. On the basis of the above, the coefficient is expressed by

$$a_0 = \begin{cases} 10^{b_1} U^{b_2} (U < 8.5) \\ 10^{b_3} U^{b_4} + b_5 (U \geq 8.5) \end{cases} \tag{3.4}$$

where the coefficient b_5 works to connect these at 8.5 m/s.

Fig. 10(c), (d), and (e) indicates behaviors of the coefficients a_1, a_2, and a_3, respectively. We consider that the continuity of GMF at $U = 0$ m/s is fulfilled and that the wind-direction dependence for low wind speeds is not significant, and we represent their behaviors by the following formulas:

$$a_1 = b_6 \left(e^{b_7 U} - 1 \right) \tag{3.5}$$

$$a_2 = b_8 U^2 + b_9 U \tag{3.6}$$

$$a_3 = b_{10} \left(e^{b_{11} U} - 1 \right). \tag{3.7}$$

An L-band GMF is formulated by using the model parameters determined above. Its three-dimensional view is shown in Fig. 11. From the figure, we can see the sigma-0 dependence on the wind speed and the wind direction. Model formulation and its coefficients are summarized in the Appendix.

E. SAR Wind Retrieval Using JERS-1 SAR

Fig. 12(a) shows a comparison of the wind speed derived from JERS-1 SAR using the L-band GMF with NSCAT and JMA buoy wind direction and NSCAT and JMA buoy wind speeds. The rms error is 2.09 m/s, and the bias is negligible (-0.0006 m/s). The SAR-derived wind speeds generally agree well with the NSCAT and JMA buoy wind speeds. Though the points scatter in a wide range for the wind speeds of 5–10 m/s, their distribution ranges become smaller for the wind speeds higher and lower than these. For wind speeds below 2 m/s, this GMF slightly underestimates them compared with those of NSCAT and the JMA buoys. It should be noted that NSCAT winds are noisy below 3 m/s. Some plots exhibit large scatter around the 20 m/s of SAR-derived wind speed. It is found that most of the large errors are the data around crosswind directions. Since, for

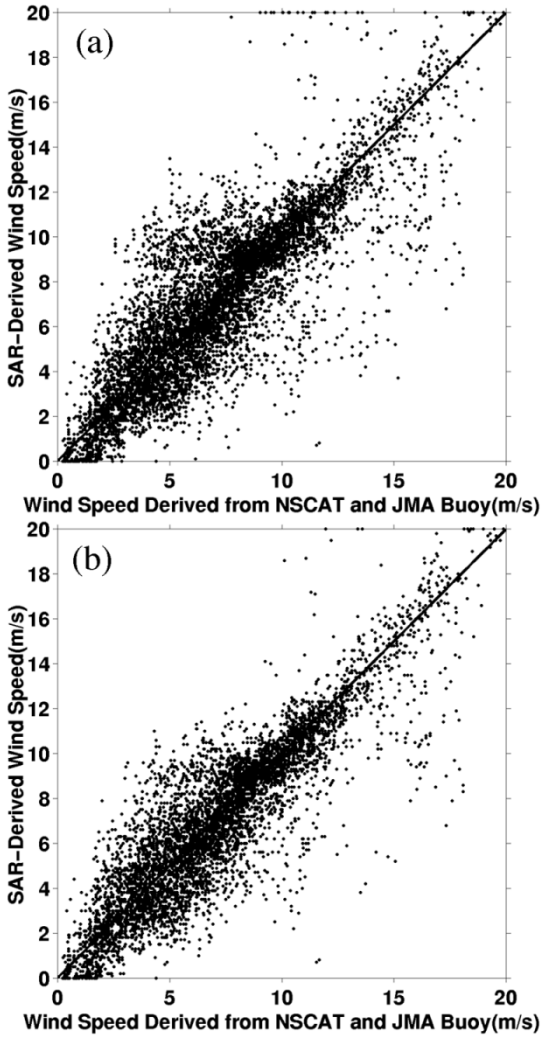

Fig. 12. (a) Comparison between SAR-derived wind speed and NSCAT and JMA buoy wind speeds. The rms error is 2.09 m/s, and the bias is -0.0006 m/s. (b) Comparison between SAR-derived wind speed and NSCAT wind speed. Crosswind data (75° to 105° and 255° to 285°), which correspond to 16% of the whole match-ups, are removed. The rms error is 1.77 m/s, and the bias is -0.12 m/s.

that specific direction, the sigma-0 dependence on wind speed is small (wind speed exponent is 0.50) compared with the other directions, small noise in the SAR sigma-0 estimate can result in large variance in the retrieved wind speed. In order to examine this consideration, we exclude the data in the range of crosswind $\pm 15°$ and compare the retrievals with the comparison data again. Fig. 12(b) shows that the SAR-derived wind speeds have less scatter and rms error of 1.77 m/s.

Now we apply the L-band GMF to the JERS-1 SAR image to generate a high spatial resolution wind-speed map. Fig. 13(a) shows one image obtained on May 18, 1997 in the Pacific. First, we subtract the estimated SAR system noise form the SAR data. Second, to reduce the speckle noise and image volume, the SAR image is averaged by 8×8 pixels, resulting in 736×640 sized pixels. Finally, we apply the L-band GMF to sigma-0 of the SAR image to convert it into the wind speed [Fig. 13(b)]. The wind directions in the image are given by the corresponding NSCAT wind vectors, which are superimposed by arrows and wind-speed values. The SAR-derived wind speed is displayed

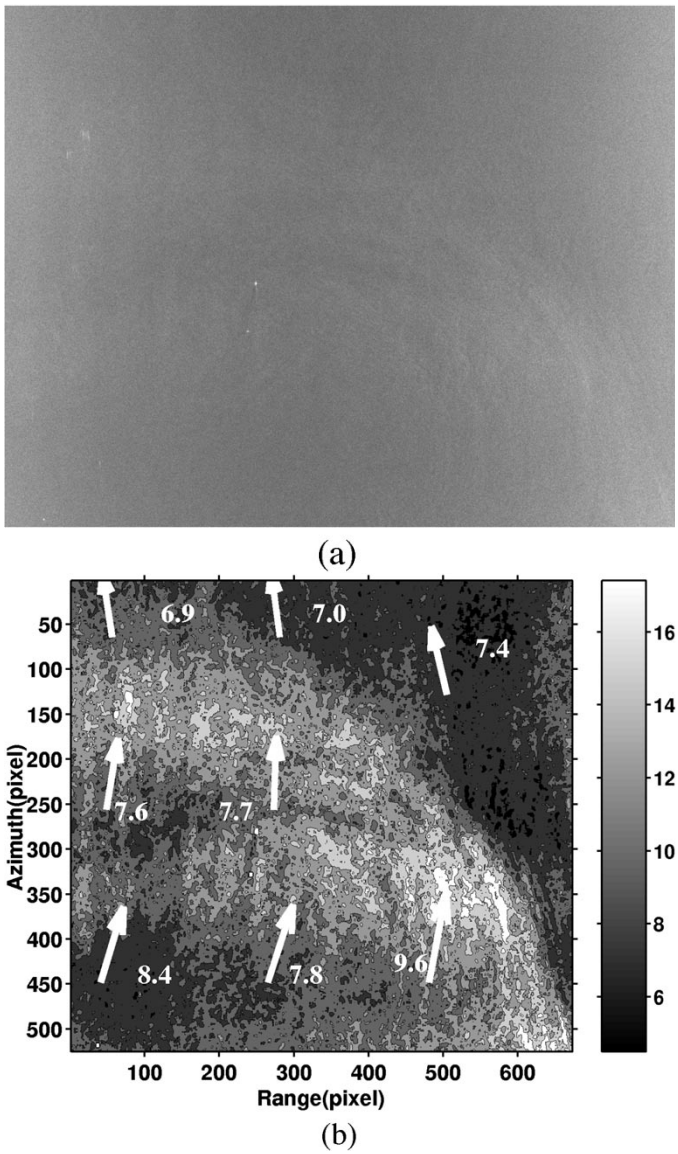

Fig. 13. (a) JERS-1 SAR image of the Pacific on May 18, 1997. (b) Wind map derived from the JERS-1 SAR image of (a). The arrows show the NSCAT wind vectors, and the value is its wind speed.

by gray tones with the scales of wind speed. They agree well with the NSCAT wind speed at the coincident points within the rms error range. Small-scale patterns in the wind-speed field are visible in the SAR image of 75-km square, which are not captured by NSCAT and probably related to mesoscale wind features. The range-dependent pattern associated with the SAR system noise is not seen, which suggests that the ocean wind signals are successfully extracted through the present methodology.

IV. Discussion

The calibration factor to convert the JERS-1 SAR 16-bit digital output from the Sigma SAR Processor to the calibrated NRCS has been proposed. The calibration factor was calculated as a comparative study of the National Space Development Agency of Japan and the Alaska SAR Facility and done by B. Chapman of the NASA Jet Propulsion Laboratory. While absolutely calibrated NRCS can be derived for bright targets, the NRCS derived from dark targets like ocean goes with the errors due to the system noise. We consider that the relative calibration of JERS-1 SAR sigma-0 conducted in the present study is a practical way for the SAR wind retrieval using JERS-1 SAR. While the incidence angle dependence of sigma-0 is possibly affected by the method of the noise removal, the derived sigma-0 has a distinct dependence of wind speed and direction, which can be considered as the representative relationship among sigma-0, wind speed, and wind direction only for an incidence angle of about 40°. There are few studies comparable with the whole results of the present study. Unal *et al.* [20] contains the L-band backscattering characteristics at the sea surface. However, since the number of used data was small, they showed only a few features of relationships among the L-band backscatter, incidence angle and ocean surface vector. The revealed features by Unal *et al.* [20] are consistent with the results of the present study in the following points; the wind exponent for the upwind, the upwind–downwind ratio, and the upwind/crosswind ratio for wind speed of 10 m/s. Phased Array type L-band Synthetic Aperture Radar onboard ALOS is planed to be launched in 2004. Since it has incidence angles ranging 8° to 60°, new research is necessary to clarify the incidence-angle characteristics and derive its GMF for wind-speed retrievals on the basis of the present study. It could also add value to other L-band microwave sensors such as the Soil Moisture and Ocean Salinity Mission and the NASA Aquarius mission, which are to be flown around 2006 for sea surface salinity retrievals.

It is known that the satellite scattrometers using the C-band (ERS-1/2 Active Microwave Instrument) and Ku-band (ADEOS-1/NSCAT, QuikSCAT/SeaWinds) have functioned well and provided global surface winds. The GMFs for the C- and Ku- bands are well validated globally. In contrast, the new L-band GMF presented here is validated only in the seas around Japan. The large number of JERS-1 SAR ocean scenes is only available within the coverage of its home receiving station. However, since the NSCAT surface winds used as the sea-truth data have been validated for the global oceans (e.g., see [21]) and we collected many match-ups in wide parameter ranges of the surface wind, the new L-band GMF may be reasonably applicable for the global oceans.

The wind retrieval error is considered to be mainly related to two problems. One is the wind direction problem. Though, in order to retrieve wind speed with high spatial resolution, we also need high spatial resolution wind direction [22], it is very difficult to obtain reliable high-resolution *in situ* surface wind data. However, for the L-band wind retrieval at low wind speeds, lack of high-resolution wind direction has less influence on the wind retrieval because the dependence of wind direction is little. For cases of high wind speeds, it can be expected that the mean wind direction does not change rapidly at such a small scale that SAR can detect. The next problem is the small-scale features, which the SAR high-resolution enables us to observe, such as depth fluctuations, currents, slicks, and fetch influence on the surface waves and radar backscattering. These appearances are enhanced in the coastal sea. In the present study, however, the influences of these features on the GMF examination may not

be significant, since all the match-ups are generated using the observations in the open oceans.

Since comparison of the three GMFs is an interesting subject, we derived wind-speed exponents of the Ku-, C-, and L-band model functions at the same incidence angle of the present study. We compute the wind speed exponent from Ku- and C-band model functions for HH polarization, Seasat-A scatterometer [17], and HH-polarization CMOD4 algorithm [6]. The upwind–downwind asymmetry is a common feature of them. While the difference in wind-speed exponent among the wind directions is relatively small for the Ku-band (1.74 –1.92), it is modest for the C-band (1.36 –1.70) and large for the L-band (0.50–2.25). Previous studies [23]–[25] have shown that the upwind–downwind contrasts are significantly enhanced for HH polarization compared to vertical–vertical polarization. It is believed that the HH cross section is much more sensitive to whitecapping and wave steepness. The difference among the three wind speed exponents suggests not only the difference of interactions between surface wave and electromagnetic wave for different wavelengths, but also the difference of the sensitivity to whitecapping and wave steepness for different wave wavelengths. As shown in Section III-D, the relationship between the coefficient a_0 of the L-band GMF and the wind speed drastically changes at around the wind speed of 8 m/s. This also suggests the effect of wave breaking and the resultant whitecapping on microwave backscattering. Improvement in understanding the physical mechanisms of the radar backscattering features is required to explain the GMF differences for the different microwave bands.

V. Summary and Conclusion

We have developed a new L-band geophysical model function using the JERS-1 SAR images. The huge volume of JERS-1 SAR data (2288 scenes) was systematically and quantitatively processed to examine the characteristics of L-band radar backscattering at the sea surface. The following results are obtained.

We estimated the SAR system noise, which has been a serious problem peculiar to the JERS-1 SAR. It is found that the system noise has a feature common in all the SAR images, and the azimuth-averaged profile of noise can be expressed as a parabolic function of range. By subtracting the estimated system noise from the SAR images, we extracted the ocean signals. This is a relative calibration of the SAR sigma-0, which enables us to examine its relationship with the surface winds quantitatively.

Using the noise-removed SAR images and the NSCAT and JMA-buoy wind vectors, we generated a match-up dataset, which contains the SAR sigma-0, the incidence angle, the wind speed, and the wind direction. Most of them are obtained in the overlapping locations of the NSCAT and JERS-1 SAR swaths. The number of generated match-ups is 7577, which enables us to perform reliable examinations of the L-band backscattering feature.

We investigated the sigma-0 dependence on the radar incidence angle, the wind speed, and the wind direction. Results of the present study indicated that dependence of sigma-0 on the incidence angle is negligible for its range of 37.0° to 42.0°. Dependence of sigma-0 on the wind speed can be well expressed by the conventional power law formula. The values of wind speed exponent are 2.25 at upwind, 0.50 at crosswind, and 1.18 at downwind. For higher wind speeds, the upwind–downwind asymmetry becomes very larger. But, for wind speeds below 8 m/s, these features are not significant.

Taking these characteristics into account, we produced a new L-band-HH GMF for SAR wind retrieval. It enables us to convert a JERS-1 SAR image into a wind-speed map. The SAR-derived wind speed has an rms error of 2.09 m/s with a negligible bias against the NSCAT wind speed comparison field.

This is the first satellite-based L-band geophysical model function proposed. Application of it to JERS-1 SAR images has proven that they can be a new source of ocean surface wind data.

Appendix
Model Formulation and Coefficients

The form of the L-band geophysical model function is

$$\sigma^0_{\text{lin}} = a_0 + a_1 \cos\phi + a_2 \cos 2\phi + a_3 \cos 3\phi$$

where ϕ is the relative wind direction. Coefficients a_0, a_1, a_2, and a_3 are functions of wind speed. They are expressed as follows:

$$\begin{aligned}
a_0 &= 10^{b_1} U^{b_2} (U < 8.5) \\
a_0 &= 10^{b_3} (U - U_0)^{b_4} + b_5 (U \geq 8.5) \\
a_1 &= b_6 (\exp(b_7 U) - 1) \\
a_2 &= b_8 U^2 + b_9 U \\
a_3 &= b_{10} (\exp(b_{11} U) - 1).
\end{aligned}$$

The threshold value is set as $U_0 = 8.5$. The coefficients b_i $(i = 1, 2, 3, \ldots, 11)$ are summarized below.

$$\begin{aligned}
b_1 &= 5.219\,429\,6 \\
b_2 &= 0.734\,326\,4 \\
b_3 &= 5.071\,137\,1 \\
b_4 &= 1.228\,200\,2 \\
b_5 &= 797\,859.7 \\
b_6 &= 41\,869.28 \\
b_7 &= 0.198\,892\,9 \\
b_8 &= 6862.769 \\
b_9 &= -49\,958.58 \\
b_{10} &= 8107.274 \\
b_{11} &= 0.167\,705\,1
\end{aligned}$$

Acknowledgment

JERS-1 SAR data were provided from National Space Development Agency of Japan through the JERS-1 science project. NSCAT wind data were obtained from the NASA Physical Oceanography Distributed Active Archive Center

(PO-DAAC). The buoy data were provided by the Japan Meteorological Agency. We appreciate useful discussions from N. Ebuchi (Hokkaido University).

REFERENCES

[1] A. Scoon, I. S. Robinson, and P. J. Meadow, "Demonstration of an improved calibration scheme for ERS-1 SAR imagery using scatterometer wind model," *Int. J. Remote Sens.*, vol. 17, pp. 413–418, 1996.

[2] W. Alpers and B. Brümer, "Atmospheric boundary layer rolls observed by the synthetic aperture radar aboard the ERS-1 satellite," *J. Geophys. Res.*, vol. 99, pp. 12 613–13 621, 1994.

[3] T. W. Vacon, O. M. Johannessen, and J. A. Johannessen, "An ERS-1 synthetic aperture radar image of atmospheric lee waves," *J. Geophys. Res.*, vol. 99, pp. 22 483–22 490, 1994.

[4] P. W. Vachon and F. W. Dobson, "Validation of wind vector retrieval from ERS-1 SAR images over the ocean," *Global Atmos. Ocean Syst.*, vol. 5, pp. 177–187, 1996.

[5] W. Alpers, U. Pahl, and G. Gross, "Katabatic wind fields in coastal areas studied by ERS-1 synthetic aperture radar imagery and numerical modeling," *J. Geophys. Res.*, vol. 103, pp. 7875–7886, 1998.

[6] F. M. Monaldo, D. R. Thompson, R. C. Beal, W. G. Pichel, and P. C.-Colòn, "Comparison of SAR-derived wind speed with model predictions and ocean buoy measurements," *IEEE Trans. Geosci. Remote Sensing*, vol. 39, pp. 2587–2600, Dec. 2001.

[7] V. Kerbaol, B. Chapron, and P. W. Vachon, "Analysis of ERS-1/2 synthetic aperture radar wave mode imagettes," *J. Geophys. Res.*, vol. 103, no. C4, pp. 7833–7846, 1998.

[8] N. W. Guinard, J. T. Ransone Jr., and J. C. Daley, "Variation of the NRCS of the sea with increasing roughness," *J. Geophys. Res.*, vol. 76, pp. 1525–1538, 1971.

[9] D. E. Weissman, D. B. King, and T. W. Thompson, "Relationship between hurricane surface wind and L-band radar backscatter from the sea surface," *J. Appl. Meteorol.*, vol. 18, pp. 1023–1034, 1979.

[10] W. C. Keller and W. J. Plant, "Cross sections and modulation transfer functions at L and ku bands mesured during the tower ocean wave and radar dependence experiment," *J. Geophys. Res.*, vol. 95, pp. 16 277–16 289, 1990.

[11] T. W. Thompson, D. E. Weissman, and F. I. Gonzalez, "SEASAT SAR cross-section modulation by surface winds: GOASEX observations," *Geophys. Res. Lett.*, vol. 8, pp. 159–162, 1981.

[12] T. W. Gerling, "Structure of the surface wind field from the seasat SAR," *J. Geophys. Res.*, vol. 91, pp. 2308–2320, 1986.

[13] B. Furevik and E. Korsbakken, "Comparison of derived wind speed from SAR and scatterometer during the ERS tandem phase," *IEEE Trans. Geosci. Remote Sensing*, vol. 38, pp. 1113–1121, Feb. 2000.

[14] M. Shimada, "Verification processor for SAR calibration and interferometry," *Adv. Space Res.*, vol. 23, no. 8, pp. 1477–1486, 1999.

[15] W. T. Liu, K. B. Katsaros, and J. A. Businger, "Bulk parameterization of air–sea exchanges in heat and water vapor including the molecular constraints at the interface," *J. Atmos. Sci.*, vol. 36, pp. 1722–1735, 1979.

[16] "Evaluation of JERS-1 SAR Data (no. 4)," Space Engineering Development Co., Ltd, Company Rep., 1995.

[17] F. J. Wentz, S. Peteherych, and L. A. Thomas, "A model function for ocean radar cross sections at 14.6 GHz," *J. Geophys. Res.*, vol. 89, pp. 3689–3704, 1984.

[18] A. Stoffelen and D. Anderson, "Scatterometer data interpretation: Estimation and validation of the transfer function CMOD4," *J. Geophys. Res.*, vol. 102, pp. 5767–5780, 1997.

[19] Ad Stoffelen. (1998) Scatterometry. [Online]. Available: http://www.library.uu.nl/digiarchief/dip/diss/01 840 669/inhoud.htm

[20] C. M. H. Unal, P. Snoeij, and P. J. F. Swart, "The polarization-dependent relation between radar backscatter from the ocean surface and surface wind vector at frequencies between 1 and 18 GHz," *IEEE Trans. Geosci. Remote Sensing*, vol. 29, pp. 621–626, Apr. 1991.

[21] N. Ebuchi, "Statistical distribution of wind speed and direction contained the preliminary nscat science data products," *J. Adv. Mar. Sci. Technol. Soc.*, vol. 3, no. 2, pp. 141–156, 1997.

[22] M. Portabella, A. Stoffelen, and J. A. Johannessen, "Toward an optimal inversion method for synthetic aperture radar wind retrieval," *J. Geophys. Res.*, vol. 107, 2002.

[23] J. Schröter, F. Feindt, W. Alpers, and W. C. Keller, "Measurement of the ocean wave-radar modulation transfer function at 4.3 GHz," *J. Geophys. Res.*, vol. 91, pp. 923–932, 1986.

[24] M. A. Donelan and W. J. Pierson Jr., "Radar scattering and equilibrium ranges in wind-generated waves with application to scatterometry," *J. Geophys. Res.*, vol. 92, pp. 4971–5029, 1987.

[25] D. G. Long, R. S. Collyer, R. Reed, and D. V. Arnold, "Dependence of the normalized radar cross section of water waves on Bragg wavelength-wind speed sensitivity," *IEEE Trans. Geosci. Remote Sensing*, vol. 34, pp. 656–666, May 1996.

Teruhisa Shimada received the B.S. and M.S. degrees in geophysics from Tohoku University, Sendai, Japan, in 1999 and 2001, respectively. He is currently pursuing the Ph.D. degree in geophysics at Tohoku University.

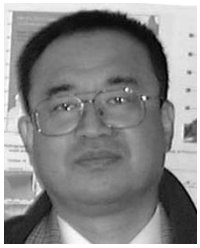

Hiroshi Kawamura (M'91) received the B.S. degree in science from Tohoku University, Sendai, Japan, in 1978 and the M.S. and Ph.D. degrees in geophysics from the Graduate School of Tohoku University.

He is currently a Professor of the Center for Atmospheric and Oceanic Studies, Faculty of Science, Tohoku University. His research interests are oceanographic application of remote sensing methods, i.e., satellite oceanography and air–sea interaction including small-scale physics at the air–sea interface.

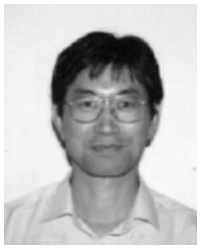

Masanobu Shimada (M'98) received the B.S. and M.S. degrees in aeronautical engineering from Kyoto University, Kyoto, Japan, in 1977 and 1979, and the Ph.D. degree in electrical engineering from the University of Tokyo, Tokyo, Japan, in 1999.

He joined the National Space Development Agency of Japan (NASDA), Tokyo, Japan, in 1979, where he designed the NASDA scatterometer. From 1985 to 1995, he developed data processing subsystems for optical and SAR data (MOS-1, SPOT, and JERS-1) at the NASDA Earth Observation Research Center (EORC), Tokyo, Japan. He was a Visiting Scientist of the Jet Propulsion Laboratory, Pasadena, CA, in 1990, where he investigated the antenna elevation pattern measurement using in-flight SAR data (SIR-B). After launch of JERS-1 in 1992, he conducted JERS-1 SAR calibration. From 1995, he has been assigned duties at EORC, where he is in charge of the JERS-1 science project. He has also managed the development of a polarimetric airborne SAR system. Since 1999, he has been a Senior Scientist and a leader of the land group. His current research interests are SAR calibration and SAR interferometric applications including polarimetric SAR interferometry.

Dr. Shimada was awarded the IEEE Interactive Session Prize at IGARSS 2000 for "Correction of the Satellite's State Vector and the Atmospheric Excess Path Delay in the SAR Interferometry: An Application to Surface Deformation Detection." He is a Chairman of the CEOS SAR CAL/VAL subgroup. He is also leading an ISPRS Commission I, WG4. He is a member of the Japan Geologic Society and the American Geophysical Union.